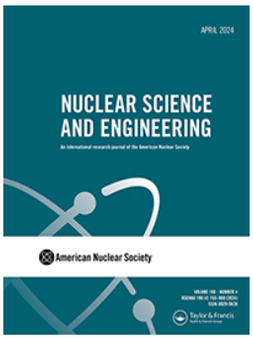

Nuclear Science and Engineering

ISSN: (Print) (Online) Journal homepage: www.tandfonline.com/journals/unse20

Measurements of the Neutron Total and Capture Cross Sections and Derivation of the Resonance Parameters of ^{181}Ta

Shunsuke Endo, Atsushi Kimura, Shoji Nakamura, Osamu Iwamoto, Nobuyuki Iwamoto, Gerard Rovira, Yosuke Toh, Mariko Segawa & Makoto Maeda

To cite this article: Shunsuke Endo, Atsushi Kimura, Shoji Nakamura, Osamu Iwamoto, Nobuyuki Iwamoto, Gerard Rovira, Yosuke Toh, Mariko Segawa & Makoto Maeda (2024) Measurements of the Neutron Total and Capture Cross Sections and Derivation of the Resonance Parameters of ^{181}Ta, Nuclear Science and Engineering, 198:4, 786-803, DOI: 10.1080/00295639.2023.2227826

To link to this article: https://doi.org/10.1080/00295639.2023.2227826

Published online: 03 Aug 2023.

NUCLEAR SCIENCE AND ENGINEERING · VOLUME 198 · 786–803 · APRIL 2024

DOI: https://doi.org/10.1080/00295639.2023.2227826

Measurements of the Neutron Total and Capture Cross Sections and Derivation of the Resonance Parameters of ^{181}Ta

Shunsuke Endo,[a]* Atsushi Kimura,[a] Shoji Nakamura,[a] Osamu Iwamoto,[a] Nobuyuki Iwamoto,[a] Gerard Rovira,[a] Yosuke Toh,[b] Mariko Segawa,[b] and Makoto Maeda[b]

[a]*Japan Atomic Energy Agency, Nuclear Data Center, 2-4 Shirakata, Tokai-mura, Naka-gun, Ibaraki 319-1195, Japan*
[b]*Japan Atomic Energy Agency, Research Group for Nuclear Sensing, 2-4 Shirakata, Tokai-mura, Naka-gun, Ibaraki 319-1195, Japan*

Received December 9, 2022
Accepted for Publication June 11, 2023

Abstract — *The neutron total and capture cross sections of ^{181}Ta were measured at the Accurate Neutron-Nucleus Research Measurement Instrument of the Materials and Life Science Experimental Facility in the Japan Proton Accelerator Research Complex to improve the accuracy of the current resonance parameters. The total cross section was determined from the transmission measurement in the energy range from 0.2 to 150 eV. The capture cross section was derived from the capture yield using the pulse height weighting technique in the energy range from thermal to 150 eV. The thermal neutron capture cross section was measured as* $21.3 \pm 0.3(stat) \pm 0.6(sys)$ *b. The obtained transmission and capture cross section were simultaneously fitted using the resonance analysis code REFIT, and the resonance parameters for resonances below 150 eV were evaluated. The present resonance parameters were compared to reported measurements.*

Keywords — *Tantalum, total cross section, capture cross section, J-PARC MLF ANNRI, resonance parameter.*

Note — *Some figures may be in color only in the electronic version.*

I. INTRODUCTION

Tantalum (Ta) has two naturally occurring isotopes, ^{180m}Ta and ^{181}Ta, in which ^{181}Ta has the largest natural abundance (99.988%). Tantalum is mixed with niobium to increase the strength of stainless steel of nuclear reactors. Leakage neutrons from reactor cores are captured by ^{181}Ta, and this reaction produces radioactive ^{182}Ta with a half-life of 115 days. The produced ^{182}Ta is one of the evaluation targets for the inventory of nuclear decommissioning. The activity concentration is subject to clearance from the International Atomic Energy Agency.[1] Therefore, many efforts are required to improve the capture cross section of ^{181}Ta.

Moreover, the 4.3-eV resonance of ^{181}Ta has been employed as reference to assess the reliability of the neutron resonance thermometry technique.[2] Since the shape of resonance changes with the temperature of a sample due to the Doppler effect, the temperature can be estimated with transmission measurements. It is required to accurately determine the shape of the 4.3-eV resonance at 0 K (i.e., resonance parameters) to obtain the temperature based on this technique.

Resonance parameters of ^{181}Ta have been determined in several experiments using the time-of-flight (TOF) method. Meaze et al.[3] measured transmission at the Pohang Neutron Facility (PNF) and determined the resonance parameters below 80 eV using the resonance analysis code SAMMY.[4] In their analyses, an inappropriate resolution function may have been adopted as indicated in Ref. [5]. This led to rather large gamma widths and smaller neutron widths than those of the other measurements (see data in Table I).

Belanova et al.[6] measured transmission from 2 to 70 eV at the SM-2 reactor in the Research Institute of Atomic Reactors (NIIAR). Resonance parameters of 4.3-eV resonance together with resonances above 40 eV were determined by area analysis, and the parameters of the other

*E-mail: endo.shunsuke@jaea.go.jp

TABLE I

Resonance Parameters of the 4.3-eV Resonance of ^{181}Ta*

Author	Resonance Energy (eV)	Γ_γ (meV)	Γ_n (meV)
Meaze et al.[3]	4.3127 ± 0.0002	139.3 ± 0.5	1.571 ± 0.002
Belanova et al.[6]	4.28 ± 0.01	65.5[a]	3.2 ± 0.1
Evans et al.[7]	4.28	62.1 ± 2.6	3.6 ± 0.1
Christensen[9]	4.29 ± 0.02	—	1.9
Wood[10]	4.282 ± 0.008	49 ± 6	3.9 ± 0.6
Shibata et al. (JENDL-4.0)[13]	4.28	53	3.2
Brown et al. (ENDF/B-VIII.0)[14]	4.28	53	3.9

*Γ_γ and Γ_n are the gamma and neutron widths, respectively.
[a]Gamma width assumed by Belanova et al.[6]

resonances were determined by shape analysis using the single-level Breit-Wigner formula.

Evans et al.[7] measured transmission, scattering, and capture reactions in the Atomic Energy Research Establishment. A simultaneous analysis[8] was applied to determine the resonance parameters of 12 resonances below 100 eV. Christensen[9] measured transmission below 50 eV using a crystal spectrometer in Brookhaven National Laboratory (BNL) and applied area analysis to determine the resonance parameters. Wood[10] measured transmission and scattering reaction using the BNL crystal spectrometer and determined the resonance parameter of the 4.3-eV resonance.

Table I shows the resonance parameters of the 4.3-eV resonance of ^{181}Ta obtained in these experiments. Resonance parameters in both JENDL-4.0 and ENDF/B-VIII.0 referred to those of Mughabghab and Garber,[11] but in JENDL-4.0 the parameters were modified from that value for the 4.3-eV resonance. Discrepancies can be observed among the reported values and evaluated libraries, especially regarding resonance widths. In a past resonance thermometry study, the transmission calculated from both JENDL-4.0 and ENDF/B-VIII.0 was compared to that obtained from experiments, and JENDL-4.0 did not agree with the experimental results.[12]

The thermal capture cross section was determined as 20.4 ± 0.2 b and 20.2 ± 0.1 b by Corte and Simonits[15] and Arbocco et al.,[16] respectively, using the activation method. Recently, Nakamura et al.[17] measured the cross section of 20.5 ± 0.4 b using the activation method at the Kyoto University Reactor (KUR). These thermal capture cross sections show good agreement. Furthermore, Schmunk et al.[18] derived the thermal capture cross section of 20.0 ± 0.9 b from extrapolation of the total cross section by the 1/v law.

In this study, we aim to improve the resonance parameters of ^{181}Ta below 150 eV. Transmission and capture cross-section measurements were performed at the Accurate Neutron-Nucleus Reaction measurement Instrument (ANNRI) of the Materials and Life Science Experimental Facility (MLF) in the Japan Proton Accelerator Research Complex (J-PARC). The thermal capture cross section was directly determined using the TOF method. The resonance parameters were determined from simultaneous fit of the transmission and capture cross section using the resonance analysis code REFIT.[19]

II. MEASUREMENTS

II.A. Experimental Procedure in ANNRI

In MLF, neutrons are produced by spallation reactions with the mercury target induced by a pulsed proton, whose intensity was 700 kW at the time of the present experiment, and repetition rate of 25 Hz. The proton beam has a double-bunch structure as shown in Ref. [5] and the pulse width of one bunch about 100 ns of the full-width at half-maximum. In ANNRI, lithium (Li)-glass and germanium (Ge) detectors[20,21] are installed at neutron flight lengths of 28.2 and 21.5 m, respectively.

Figure 1 displays the top view of ANNRI. In the transmission measurements, the sample was placed at the upstream of the collimator to reduce the gamma rays and scattered neutron from the sample to negligible levels. Two types of Li-glass detectors, GS20 and GS30,

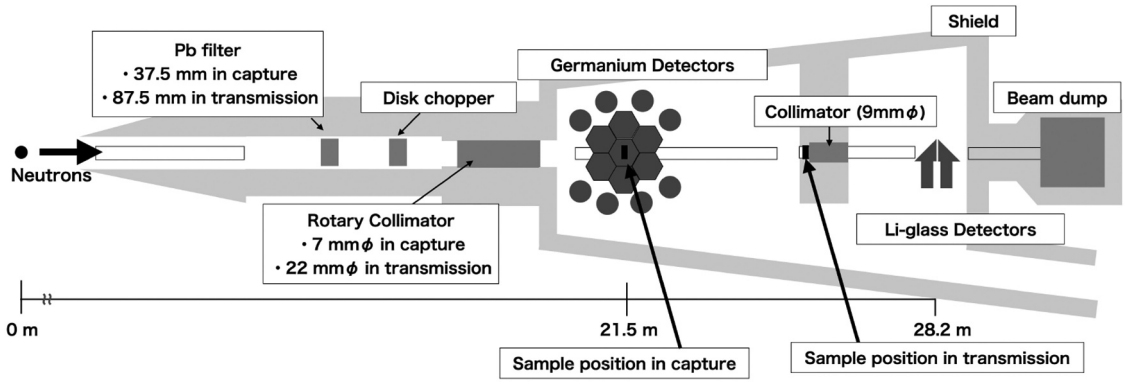

Fig. 1. Overview of ANNRI.

were utilized to measure the neutron transmission. GS20 consists of a ^{6}Li-enriched scintillator and photomultiplier (PMT H7195) that exhibits high sensitivity to neutrons owing to the large cross section of the $^{6}\mathrm{Li}(n,\alpha)^{3}\mathrm{H}$ reaction. Moreover, GS30 comprises a ^{7}Li-enriched scintillator and, therefore, displays a very low sensitivity to neutrons. The TOF spectrum by GS30 was employed to remove gamma-ray background events from that by GS20. The CAEN V1720 (12-bit, 250-MHz) module was used for data acquisition, and the pulse height (PH) and TOF were recorded in the list mode.

For the capture cross-section measurements, Ge detectors were used to detect gamma rays emitted from neutron capture reactions. CAEN V1724 modules were employed to acquire the PH and TOF in the list mode. Note that other details of the transmission and capture cross-section measurements at ANNRI are available in Ref. [5].

II.B. Samples

For the transmission measurements, three metal samples of ^{nat}Ta with the same chemical composition and thicknesses of 25 μm, 100 μm, and 2 mm were used. The areal densities of these samples are listed in Table II. The impurities on elements in the samples are also summarized in Table III. The areal densities were calculated from the theoretical density and the thickness measured by a micrometer. In the present experiment, sample-in and sample-out (so-called blank) measurements were performed. In addition to them, measurements with a notch filter consisting of silver, manganese, cobalt, and indium were made to correct the difference of detection efficiencies between GS20 and GS30 using black resonances.

For the capture cross-section measurements, a natural Ta sample with area of 12.33 mm^2 and thickness of 6 μm and a gold (Au) sample were used. A boron sample was employed to determine an incident neutron fluence rate via the $^{10}\mathrm{B}(n,\alpha\gamma)^{7}\mathrm{Li}$ reaction. This is a commonly used technique since the events from this reaction are very easy to separate from background events because of its large cross section with the emission of the single-energy gamma ray (478 keV). Moreover, the sample-dependent and sample-independent backgrounds were estimated using carbon-sample and blank measurements, respectively. Table IV lists the masses and areal densities of these samples. The area was measured with an accurate imaging technique using an IM-6140 device supported by KEYENCE Co. LTD.

TABLE II

Information of the Ta Samples for the Transmission Measurements

Thickness	Areal Density (atom/b)
25 μm	$(1.20 \pm 0.05) \times 10^{-4}$
100 μm	$(5.13 \pm 0.11) \times 10^{-4}$
2 mm	$(1.168 \pm 0.001) \times 10^{-2}$

TABLE III

Impurities in the Ta Samples

Element	Ratio (ppm)
Niobium	256
Tungsten	130
Oxygen	98
Carbon	38
Nitrogen	17
Molybdenum	12
Others	19

TABLE IV

Sample Information in the Capture Cross-Section Measurements

Sample	Mass (mg)	Areal Density (atom/b)
Tantalum, 6-μm thickness	1.123 ± 0.001	$(3.031 \pm 0.002) \times 10^{-5}$
Gold	15.038 ± 0.001	$(3.202 \pm 0.002) \times 10^{-4}$
Carbon	5.644 ± 0.001	$(1.83 \pm 0.01) \times 10^{-3}$
Boron	1.963 ± 0.001	$(5.76 \pm 0.06) \times 10^{-4}$

III. TOF DATA ANALYSES

III.A. Transmission Analysis

The neutron total cross section was determined in off-line analysis of the measured data with both the GS20 and GS30 detectors. Figure 2 shows the PH spectra of each detector in the measurement with the 2-mm-thick Ta sample.

A detection threshold of PH spectra was set at 140 ch. to reduce the influence of background events. The peak around 220 ch. was produced by the ^{6}Li$(n,\alpha)^3$H reaction. This peak was also observed in the GS30 spectrum since this detector contains ^{6}Li with the concentration of about 0.01%. This amount of ^{6}Li was small enough to be negligible in the derivation of the transmission. "Double hit" means a pileup event in which two neutron detections occurred within a short time window and, hence, overlapped. A dead-time effect due to the time window in data acquisition was corrected by an extended dead-time model.

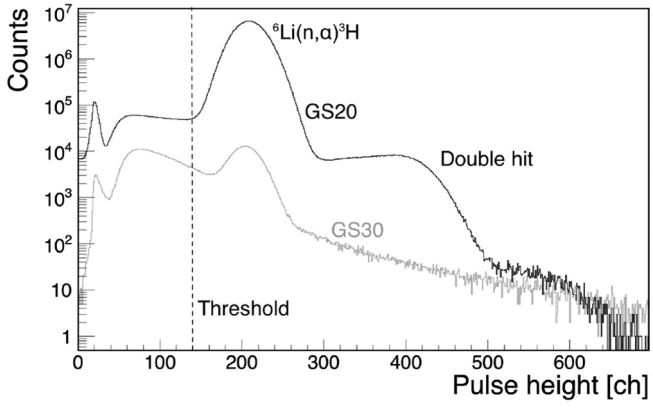

Fig. 2. Pulse height spectra of the GS20 and GS30 detectors in the measurement with the 2-mm-thick Ta sample. The gamma-ray peaks of the ^{6}Li$(n,\alpha)^3$H reaction were found in the GS20 and GS30 spectra. The vertical dashed line at 140 ch. shows the detection threshold.

The details of the dead-time correction are described in Sec. 3.2 in Ref. [5]. Figure 3 shows the TOF spectra measured with the GS20 and GS30 detectors after the dead-time correction for the 2-mm-thick Ta measurement.

The frame-overlap background was caused by slow neutrons with the TOF more than 40 ms mixing into the next pulse. This background layer, which also includes constant backgrounds caused by the environmental radiation and noise, was subtracted as follows. The TOF spectrum of the GS20 detector was fitted in the region from 37 to 40 ms, where neutrons were cut by a disk chopper, using an exponential function: $p_1 \exp(-p_2 t) + p_3$, where p_1, p_2, and p_3 are fitting parameters and t is TOF. In the case of the GS30 detector, a constant component p_3 was enough to express the background since the detector has low neutron sensitivity. The estimated frame-overlap background is shown in Fig. 3. The frame-overlap background had little influence on the derivation of transmission.

The gamma-ray background from other than the Ta sample was removed by subtracting the spectrum of the GS30 detector from that of the GS20 one, as mentioned before. Figure 4 displays the spectra of the GS20 and GS30 detectors in the notch filter–inserted measurement. To correct a difference in detection efficiencies, the GS30 spectrum was multiplied by a factor of 1.78 ± 0.04, which was determined using the dips of the black resonances measured with the GS20 detector. The background events caused by small-angle scattered neutrons and capture gamma rays from the sample were negligible since these were eliminated by a collimator installed between the sample and the detector.

Finally, the transmission was determined by dividing the TOF spectrum with the Ta sample by that without the sample. Further details are described in Ref. [5]. The reduced total cross section, $\widetilde{\sigma}_{tot}$, was defined as the total cross section broadened with the resolution function and the Doppler effect, and it was obtained from the transmission T and the areal density, n_{Ta}, as

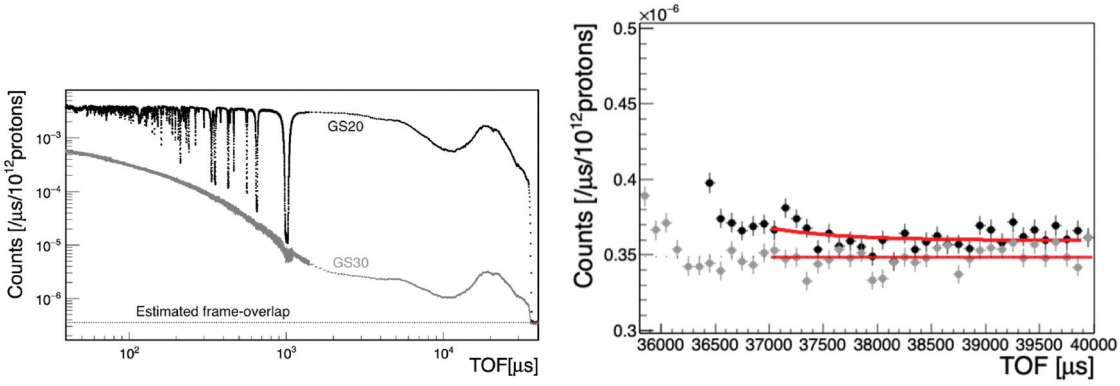

(a) Overall view. (b) Enlarged view around fitting region.

Fig. 3. TOF spectra of the GS20 and GS30 detectors after the dead-time correction for the 2-mm-thick Ta measurement. The dotted line is estimated frame-overlap background of the GS20 spectrum by fitting the spectrum from 37 to 40 ms.

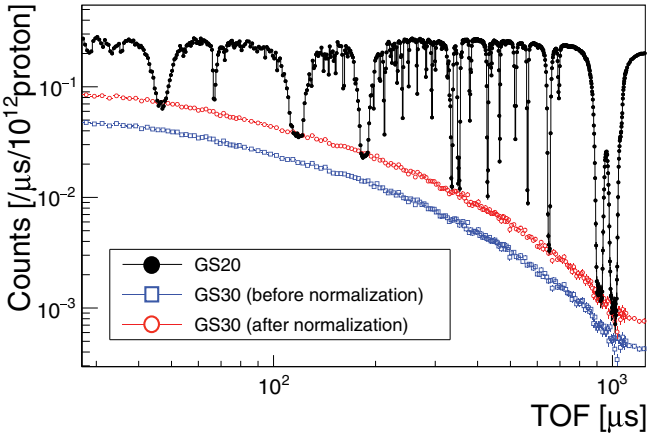

Fig. 4. TOF spectra of the GS20 and GS30 detectors in the notch filter–inserted measurement. The spectra of the GS30 detector before and after normalization are shown.

$$\widetilde{\sigma}_{tot}(E_n) = -\frac{1}{n_{\mathrm{T_a}}} \ln\, T(E_n) \ . \qquad (1)$$

III.B. Capture Cross-Section Analysis

The pulse height weighting technique (PHWT)[22] was applied to derive the capture cross section. The weighted spectrum can be written as follows:

$$S(E_n) = \frac{1}{P} \sum_{E_\gamma} \frac{W(E_\gamma) R(E_\gamma, E_n)}{B_n + E_n} \ , \qquad (2)$$

where P = number of incident protons; E_γ and E_n = gamma-ray and neutron energies, respectively; B_n = neutron binding energy; $R(E_\gamma, E_n)$ = number of detected events; $W(E_\gamma)$ = weighting function. The weighting function was calculated considering the response functions of the Ge detector, similar to that in the previous study[5] as

$$W(E_\gamma) = N\Big\{-1.059 \times 10^2 \sqrt{E_\gamma} + 25.18 E_\gamma + 0.4569 E_\gamma^{3/2} - 6.753 \times 10^{-3} E_\gamma^2 + 2.455 \times 10^{-5} E_\gamma^{5/2}\Big\} \ , \qquad (3)$$

where N is the normalization factor and E_γ is in units of kilo-electron-volts. For the capture cross section of Au, the normalization factor was determined to reproduce the thermal value of JENDL-4.0. The correction factor and uncertainty caused by the difference in gamma-ray distributions between Ta and Au were obtained as follows. In this analysis, events only above 600 keV were adopted because there were many background gamma rays in the 511-keV and lower-energy regions.

Figure 5 shows the gamma-ray spectra $\sum_{E_n} R(E_\gamma, E_n)$ of Ta and Au. The lower limit of deposited energy in the Ge detectors was set at 200 keV in this measurement. To estimate the difference in the gamma-ray spectrum below the lower limit, the spectra were fitted by an exponential function f_{exp} from 250 to 500 keV and by a constant value f_{const} from 200 to 250 keV. The fitting range was determined by the lower limit and the absence of the influence of the 511-keV peak.

The fitting results are shown in Fig. 5 and used as the gamma-ray distribution below the lower limit. The weighted integral values of the two fitting results between 0 and 250 keV are defined as

$$I_1^{\mathrm{exp}} = \int_0^{250} f_{\mathrm{exp}}(E_\gamma) W(E_\gamma) dE_\gamma,$$
$$I_1^{\mathrm{const}} = \int_0^{250} f_{\mathrm{const}}(E_\gamma) W(E_\gamma) dE_\gamma \ . \qquad (4)$$

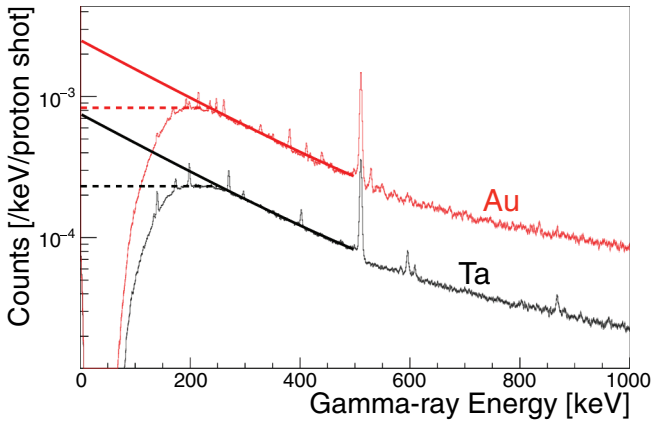

Fig. 5. Extrapolation of PH spectra below the detection threshold for Ta and Au. The results fitted to the PH spectra by the exponential function and the constant value are shown by solid and dotted lines, respectively.

Here, the weighted integral values are used instead of just the integral value because each event is summed up by weighting with its gamma-ray energy as shown in Eq. (2). For gamma rays with energies higher than the lower limit, the weight integral values are similarly defined as

$$I_2 = \sum_{E_\gamma=250}^{600} \sum_{E_n} R(E_\gamma, E_n) W(E_\gamma),$$
$$I_3 = \sum_{E_\gamma=600}^{B_n} \sum_{E_n} R(E_\gamma, E_n) W(E_\gamma) \ . \quad (5)$$

The correction factor C_{PHWT} of the cross section is obtained as

$$C_{\mathrm{PHWT}} = \frac{I_{3,\mathrm{Ta}}}{I^{\mathrm{exp}}_{1,\mathrm{Ta}} + I_{2,\mathrm{Ta}} + I_{3,\mathrm{Ta}}} \Big/ \frac{I_{3,\mathrm{Au}}}{I^{\mathrm{exp}}_{1,\mathrm{Au}} + I_{2,\mathrm{Au}} + I_{3,\mathrm{Au}}} \ . \quad (6)$$

Since events only above 600 keV were considered in this analysis, this correction factor refers to the number ratio of the analyzed events to all events for Ta and Au. The uncertainty of PHWT was evaluated from the differences in the gamma-ray spectrum below 600 keV. Therefore, the uncertainty was estimated as

$$\sqrt{\Delta I^2_{\mathrm{Ta}} + \Delta I^2_{\mathrm{Au}}} \ , \quad (7)$$

where ΔI_i is calculated by

$$\Delta I_i = \frac{I^{\mathrm{exp}}_{1,i} + I_{2,i}}{I^{\mathrm{exp}}_{1,i} + I_{2,i} + I_{3,i}} - \frac{I^{\mathrm{Const}}_{1,i} + I_{2,i}}{I^{\mathrm{Const}}_{1,i} + I_{2,i} + I_{3,i}}$$
$$(i = \mathrm{Ta\ or\ Au}) \ . \quad (8)$$

This represents the difference in the estimation of the unobserved gamma-ray distribution at lower energies than the lower limit. The correction factor and relative uncertainty are obtained as $C_{\mathrm{PHWT}} = 0.893$ and 2.5%, respectively.

The dead-time correction was applied with the extended dead-time model, in a similar way to the transmission analysis. The frame-overlap and constant backgrounds were estimated by fitting the spectrum after 40.0 ms with the exponential function: $p_1 \exp(-p_2 t) + p_3$, where p_1, p_2, and p_3 are the fitting parameters. In MLF, neutrons are not always provided every 40.0 ms (25 Hz) because some of the proton pulses are also sent to the other facility at a specific allocation rate; MLF : the other = 126 : 4 during the present experiment, making a TOF spectrum beyond 40.0 ms (namely, the frame-overlap spectrum). Therefore, when the protons were provided to the other facility, the frame-overlap TOF spectrum could be measured, expressing the influence of the overlapping neutrons from preceding proton pulses. The details of the frame-overlap correction are described in Sec. 4.3.1 of Ref. [5]. Figure 6 shows the frame-overlap spectrum shifted by 40 ms and multiplied by 126. The dotted line is the fitting result, and the frame-overlap correction was performed by subtracting the fitting result from the TOF spectrum.

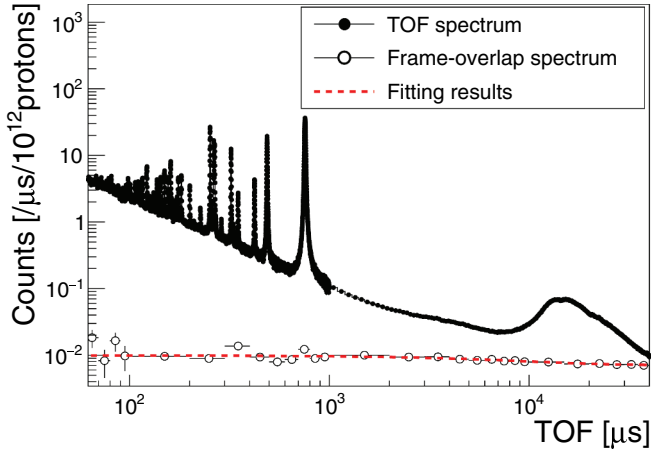

Fig. 6. TOF spectrum of the Ta sample in the capture cross-section measurement. The dotted line is the fitting results of frame-overlap spectrum shifted by 40 ms.

The sample-independent background and the background events caused by scattered neutrons in the sample were estimated using the spectra of the blank and carbon measurements, respectively. The capture yield Y_{Ta} is written as

$$Y_{\mathrm{Ta}}(E_n) = (S_{\mathrm{Ta}}(E_n) - S_{Blank}(E_n)) - \frac{n_{\mathrm{Ta}}\,\widetilde{\sigma}_{s,\mathrm{Ta}}(E_n)}{n_{\mathrm{Carbon}}\,\widetilde{\sigma}_{s,\mathrm{Carbon}}(E_n)}(S_{\mathrm{Carbon}}(E_n) - S_{Blank}(E_n)) \ , \quad (9)$$

where $S(E_{\mathrm{n}})$ = weighted spectrum after the frame-overlap correction; n_{Ta} = areal density of the Ta sample; $\widetilde{\sigma}_{s,\mathrm{Ta}}(E_n)$ = scattering cross section of Ta considering the resolution function of ANNRI derived by Kino et al.[23] In order to consider the self-shielding effect, the number of scattering events obtained from the particle and heavy ion transport code system (PHITS) simulation[24] with JENDL-4.0 was used instead of the cross section. The number of escaped neutrons from the sample after scattering was estimated for each neutron energy.

Figure 7 displays the TOF spectra of Ta [$S_{\mathrm{Ta}}(E_n)$], blank [$S_{Blank}(E_n)$], and normalized carbon spectrum [the second term in the right-hand side of Eq. (9)]. The normalized carbon was obtained by normalizing the carbon spectrum with the ratio of $\widetilde{\sigma}_{s,\mathrm{Ta}}(E_n)$ for carbon and Ta, taking into account the areal density. Thus, it means the scattering backgrounds of Ta.

The neutron fluence rate $\phi(E_n)$ was derived from the measurement with the boron sample. The dead-time correction and background subtraction were applied to the TOF spectrum of the boron sample using the previously explained method. The neutron

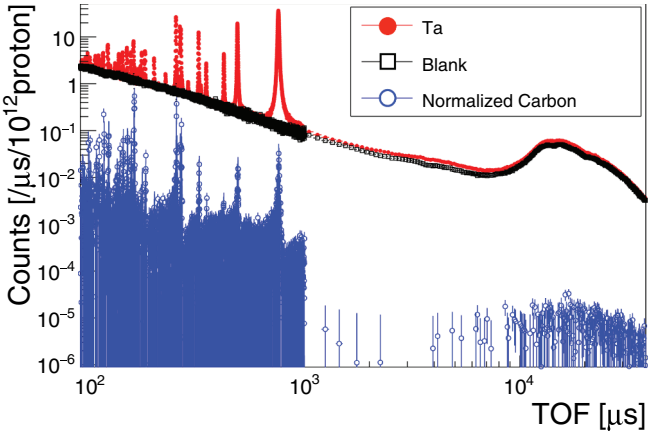

Fig. 7. TOF spectra of the Ta, blank, and normalized carbon.

self-shielding and multiple-interaction effects were estimated by simulations using the PHITS code[24] and were used to deduce a correction factor as a function of TOF. After the self-shielding and multiple-interaction correction, the spectrum was divided by the $^{10}\mathrm{B}(n,\alpha\gamma)$ reaction cross section to obtain the neutron fluence rate.

Finally, to obtain the normalization factor N in Eq. (3), the capture yield at the thermal neutron energy was determined from fitting the yields between 16.8 to 152 meV with the $1/v$ law. The self-shielding effect at the thermal neutron energy was estimated by PHITS simulation. The reduced capture cross section was obtained as

$$\widetilde{\sigma}_{cap}(E_n) = \frac{C_{\mathrm{PHWT}}}{n_{\mathrm{Ta}}\phi(E_n)}\,Y_{\mathrm{Ta}}(E_n) \ , \quad (10)$$

where C_{PHWT} = correction factor of PHWT defined in Eq. (6); n_{Ta} and Y_{Ta} = areal density and capture yield of the Ta sample, respectively; $\phi(E_n)$ = neutron fluence rate.

III.C. Resonance Analysis

The resonance parameters were determined from simultaneous fit of one capture cross section and three transmission measurements using the resonance analysis code REFIT.[19] The self-shielding and multiple-interaction effects of the capture cross section were considered with the corresponding functions of REFIT. The resolution function of Kino et al.[23] and the structure of the proton pulses were also taken into account. Doppler broadening was considered assuming the ideal gas model, in which the effective temperature was fixed at 25.3 meV. Small resonances, whose capture cross section is smaller than about 30 b, were not analyzed, or only the neutron width was fitted because of a lack of statistics in the capture measurements. Moreover, the 85.1- and 85.6-eV resonances were not fitted because these resonances overlapped each other. These resonance parameters without fitting were taken from JENDL-4.0 for ^{181}Ta. The impurities ^{nat}W and ^{180m}Ta were considered using JENDL-4 and JEFF-3.3, respectively, while effects of the other impurities were negligible due to their low-resonance cross sections. Transmissions of the 25- and 100-μm-thick measurements in the energy range from 0.01 to 1 eV were not used in the resonance analysis because systematic uncertainty caused by neutron beam intensity fluctuation was extremely large. Transmission below 0.2 eV was not also used for the fit because neutron diffraction was observed.

IV. RESULTS

IV.A. Total Cross Section

The reduced total cross section is shown in Fig. 8. The systematic uncertainty for the reduced total cross section comes from the dead-time correction, the normalization factor of the GS30 detector, the sample thickness, and the neutron beam intensity. The neutron beam intensity at the detector position changed because of fluctuation of the proton beam power and neutron scattering with air on the neutron beam line. In ANNRI, the length of the air region is 7 m. The fluctuation of the proton beam power was corrected by proton current measured by a current transformer monitor in MLF. On the other hand, the fluctuation caused by the neutron scattering with air could not be monitored. Since the neutron scattering with air depends on atmospheric pressure and humidity, the uncertainty of beam intensity was estimated as 0.3% with the two parameters. The details of the estimation are described in the Appendix.

IV.B. Capture Cross Section

Figures 9 and 10 display the reduced capture cross section along with statistical and various systematic uncertainties. The thermal capture cross section of $21.3 \pm 0.3\ (stat) \pm 0.6\ (sys)$ b was obtained by fitting the capture yield with the $1/v$ law, and this result is in good

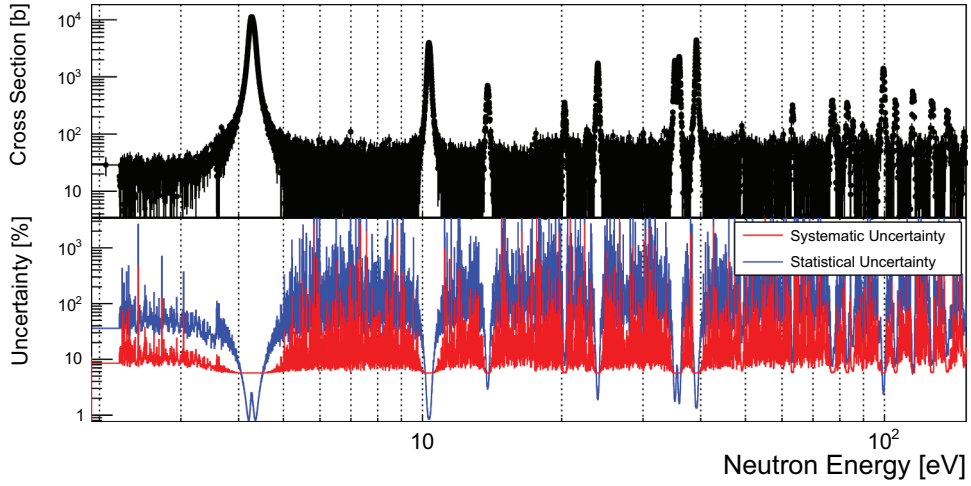

Fig. 8. Reduced total cross section (top) and uncertainties (bottom) of natural Ta obtained from the Ta 100-μm-thick measurement.

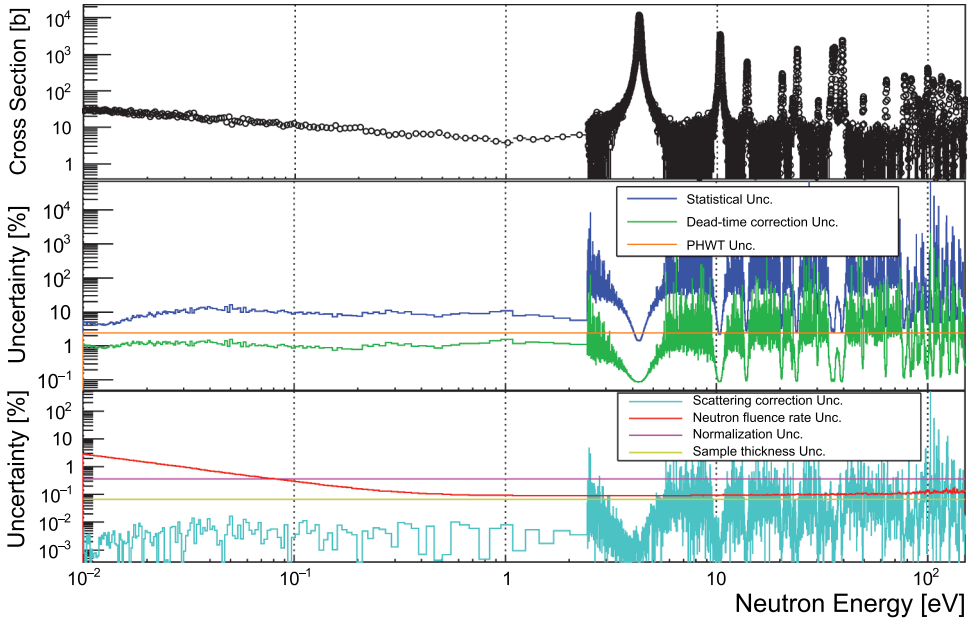

Fig. 9. Reduced capture cross section from 10 meV to 150 eV with uncertainties.

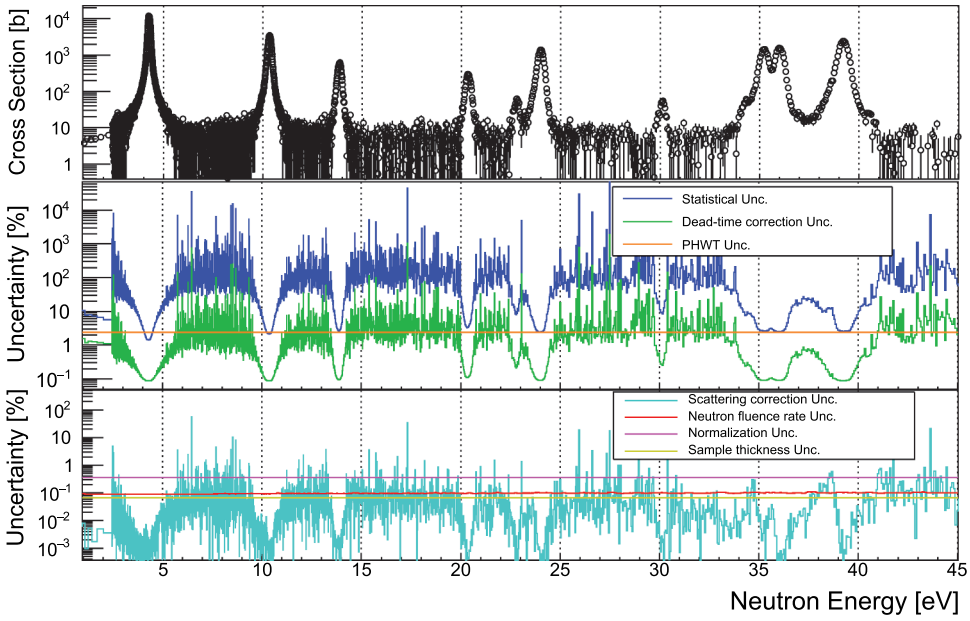

Fig. 10. Reduced capture cross section from 1 to 45 eV with uncertainties.

agreement with past data by the activation method, 20.5 ± 0.4 b by Nakamura et al.[17] The effect of impurities is negligible at thermal neutron energy of about 0.003 b. The neutron fluence rate uncertainty represents the uncertainty of the measurement with the boron sample, including the statistical correction (0.1%), dead-time correction (0.1%), scattering correction (< 0.1%), and self-shielding correction (1.1%) uncertainties at the thermal energy.

IV.C. Resonance Parameters

The results of the resonance analysis are shown in Figs. 11 and 12, and the obtained resonance parameters are listed in Table V together with the parameters in the past measurements and evaluated libraries. The past data are taken from Meaze et al.,[3] Belanova et al.,[6] Evans et al.,[7] Christensen,[9] Wood,[10] Desjardins et al.,[25] Fluharty et al.,[26] Firk,[27] and Tsubone et al.[28] The description "fixed" in Table V means the parameters that were not fitted. The capture kernel was caluculated as $g\Gamma_\gamma\Gamma_n/(\Gamma_\gamma+\Gamma_n)$, where Γ_n was derived from $g\Gamma_n$ using the spin J. For previous studies where J was unknown, the values in JENDL-4.0 were used.

V. DISCUSSION

Many resonance parameters obtained in this study are different from those of Meaze et al.[3] and Christensen.[9] As discussed in Ref. [5], the time

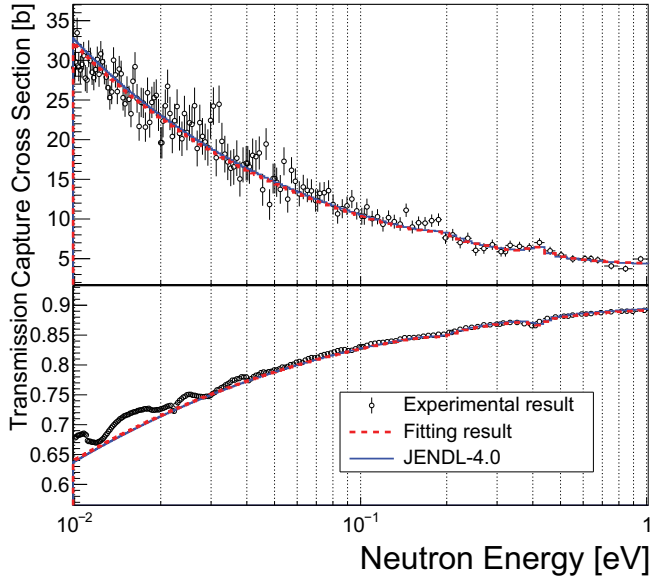

Fig. 11. Transmission, capture cross section, fitting results, and JENDL-4.0 from 0.01 to 1 eV.

distribution of the neutron beam in PNF was broader than that in MLF. In PNF, neutrons were produced from bremsstrahlung by the pulsed electrons accelerated up to 100 MeV by the linac,[29] and the electron width was 1 μs, which is broader than the proton width in MLF. Moreover, the adopted resolution function might be too simple to express measured resonance shapes. Therefore, the influence of the experimental resolution on their derivation of resonance parameters was very large. For Christensen,[9] details on the resolution

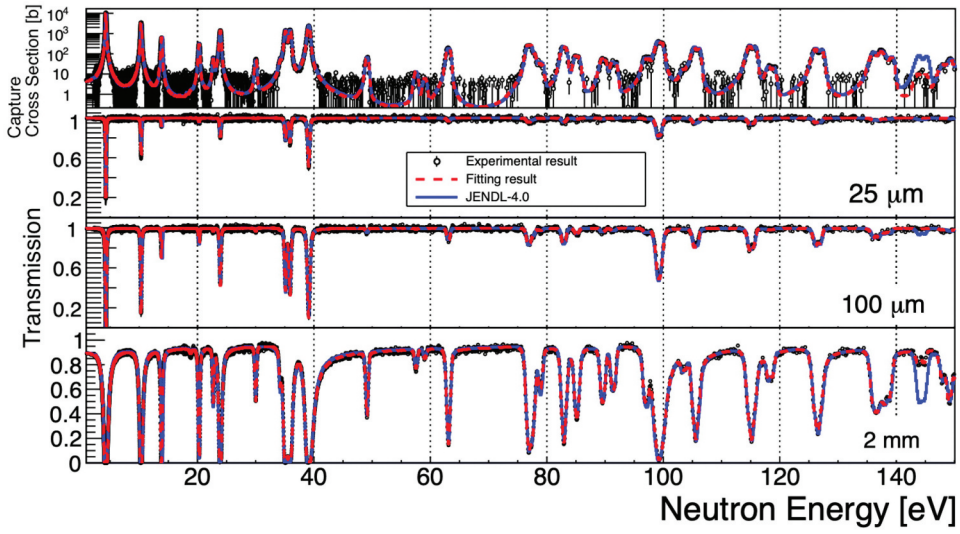

Fig. 12. Transmission, capture cross section, fitting results, and JENDL-4.0 from 1 to 150 eV.

function were not described. According to Ref. [30], the resolution at 5 eV was 0.26 eV in the crystal spectrometer of BNL, and this value was much larger than 0.04 eV at 5 eV in MLF. Since this value is about half the width of the 4.3-eV resonance of Ta, it is considered that the resolution affected the derivation of the resonance parameters.

Figure 13 shows the ratio of the capture kernel $g\Gamma_\gamma\Gamma_n/(\Gamma_\gamma+\Gamma_n)$ to the present results. It is clear that the present results are in almost good agreement with those of Evans et al., Belanova et al., Desjardins et al., and Wood within uncertainties except for Meaze et al., which make the overall underestimation. Regarding the 4.3-eV resonance, the obtained resonance parameters are in good agreement with those reported by Wood.[10] The present capture kernel is consistent with the result of Evans et al.,[7] although Evans et al. provide a rather large gamma width. Belanova et al.[6] give a slightly smaller capture kernel with an assumed gamma width (65.5 meV). The present capture kernel of the 10.3-eV resonance is larger than those of the past measurements because of the larger neutron width. The neutron width of the present result is close to that of ENDF/B-VIII.0.

The present neutron width of the 144-eV resonance was smaller than that reported by Tsubone et al.[28] by a factor of 10, although Tsubone et al.[28] assumed a reasonable value (55 meV) for the gamma width. The cross section of the 144-eV resonance calculated from the parameters of Tsubone et al. was larger than our measured data. This fact is supported by agreement with the results reported by Desjardins et al.[25] The present result suggests that the neutron width of JENDL-4.0 is too large and should be revised.

In the neutron energy region below 1 eV, the resonances (0.2 and 0.4 eV), which were expected to be those of ^{180m}Ta, are found in Fig. 11. However, since the statistics of the capture events were not high enough, the resonance parameters could not be determined. The energy of the 0.4-eV resonance might be slightly lower because there was a discrepancy in the dip position between the obtained transmission and the the evaluated library (JEFF-3.3) as shown in Fig. 11.

In this analysis, the parameters of the negative resonance were varied to adjust the cross section in the low-energy region shown in Fig. 11. The neutron widths of two negative resonances were different from JENDL-4.0. Instead of an increase in the neutron width of the −44-eV resonance, the one of the −12-eV resonance was decreased. Since the correlation between these parameters was 79%, it was difficult to uniquely determine each parameter in this analysis. Additional analysis and the other experiment would be needed to determine the parameters of the negative resonance.

Figures 14 and 15 compare the capture cross section calculated from the obtained resonance parameters $\sigma_{present}$ with that of the evaluated libraries $\sigma_{evaluation}$. The residual is defined as $(\sigma_{evaluation}-\sigma_{present})/\sigma_{present}$. For the 4.3-eV resonance, JENDL-4.0 underestimates the peak cross section by approximately 2000 b, i.e., 10%. On the other hand, the present peak cross section

TABLE V

Resonance Parameters of ^{181}Ta*

Number	Reference	J/l	Resonance Energy (eV)	Γ_γ (meV)	$g\Gamma_n$ (meV)	Capture Kernel (meV)
	Present work	4/0	−44.0 (fixed)	55.0 (fixed)	171 ± 2	
	JENDL-4.0	4/0	−44.0	55.0	112.5	
	Present work	3/0	−11.7 (fixed)	55.0 (fixed)	5.22 ± 0.19	
	JENDL-4.0	3/0	−11.7	55.0	9.06	
1	Present work	4/0	4.2769 ± 0.0003	49.1 ± 0.1	2.075 ± 0.005	1.930 ± 0.004
	Meaze et al.	4/0	4.3127 ± 0.0003	139.3 ± 0.5	0.8837 ± 0.001	0.874 ± 0.001
	Belanova et al.	—	4.28 ± 0.01	65.5 (fixed)	1.81 ± 0.06	1.73 ± 0.05
	Evans et al.	4/0	4.28	62.1 ± 2.6	2.01 ± 0.06	1.90 ± 0.05
	Christensen	—	4.29 ± 0.02	—	1.0	—
	Wood	4/0	4.282 ± 0.008	49 ± 6	2.19 ± 0.3	2.03 ± 0.26
	JENDL-4.0	4/0	4.28	53.0	1.80	1.70
	ENDF/B-VIII.0	4/0	4.28	53.0	2.19	2.04
2	Present work	3/0	10.329 ± 0.001	51.7 ± 0.2	2.202 ± 0.008	2.006 ± 0.006
	Meaze et al.	3/0	10.3991 ± 0.0014	205.4 ± 4.0	0.972 ± 0.003	0.962 ± 0.003
	Belanova et al.	—	10.37 ± 0.03	76.5 ± 3.5	1.68 ± 0.07	1.60 ± 0.06
	Evans et al.	4/0	10.40	65.0 ± 6.0	2.03 ± 0.06	1.92 ± 0.05
	Christensen	—	10.36 ± 0.05	-	1.3	—
	JENDL-4.0	3/0	10.36	65.0	1.75	1.65
	ENDF/B-VIII.0	3/0	10.34	55.0	2.04	1.88
3	Present work	4/0	13.832 ± 0.001	51.6 ± 0.4	0.533 ± 0.002	0.523 ± 0.002
	Meaze et al.	4/0	13.9270 ± 0.0043	155.4 ± 12.2	0.420 ± 0.005	0.418 ± 0.005
	Belanova et al.	—	13.89 ± 0.06	57.4 ± 3.3	0.50 ± 0.02	0.49 ± 0.02
	Evans et al.	4/0	13.95	52.0 ± 2.6	0.57 ± 0.02	0.56 ± 0.02
	Christensen	—	13.9 ± 0.1	—	0.7	—
	JENDL-4.0	4/0	13.95	54.0	0.570	0.559
	ENDF/B-VIII.0	4/0	13.95	52.0	0.570	0.559
4	Present work	3/0	20.293 ± 0.001	55.5 ± 0.6	0.456 ± 0.001	0.448 ± 0.001
	Meaze et al.	3/0	20.4213 ± 0.0078	195.0 ± 4.3	0.372 ± 0.004	0.370 ± 0.004
	Belanova et al.	—	20.35 ± 0.07	51.8 ± 4.5	0.48 ± 0.02	0.47 ± 0.02
	Evans et al.	3/0	20.2	70 ± 6	0.53 ± 0.03	0.52 ± 0.03
	Christensen	—	20.7	—	0.6	—
	JENDL-4.0	3/0	20.29	52.0	0.480	0.470
	ENDF/B-VIII.0	4/0	20.3	60.0	0.575	0.565
5	Present work	3/0	22.717 ± 0.002	59.6 ± 2.6	0.0933 ± 0.0007	0.0930 ± 0.0007
	Meaze et al.	3/0	22.9437 ± 0.0020	254.9 ± 10.2	0.183 ± 0.004	0.183 ± 0.004
	Belanova et al.	—	22.78 ± 0.09	65.7 ± 10.0	0.10 ± 0.01	0.10 ± 0.01
	JENDL-4.0	3/0	22.72	60.0	0.105	0.10
	ENDF/B-VIII.0	3/0	22.7	52.0	0.110	0.25
6	Present work	4/0	23.934 ± 0.001	54.3 ± 0.4	3.21 ± 0.02	2.90 ± 0.01
	Meaze et al.	4/0	24.0589 ± 0.0011	252.2 ± 5.4	1.478 ± 0.015	1.46 ± 0.01
	Belanova et al.	—	24.00 ± 0.09	76.4 ± 7.3	2.53 ± 0.19	2.39 ± 0.17
	Evans et al.	4/0	23.9	59.8 ± 3.2	3.3 ± 0.1	3.01 ± 0.08
	Christensen	-	24.2 ± 0.2	—	2.5	—
	JENDL-4.0	4/0	23.92	62.0	2.90	2.68
	ENDF/B-VIII.0	3/0	23.9	53.0	3.25	2.85

(Continued)

TABLE V (Continued)

Number	Reference	J/l	Resonance Energy (eV)	Γ_γ (meV)	$g\Gamma_n$ (meV)	Capture Kernel (meV)
7	Present work	3/0	30.026 ± 0.002	61.7 ± 3.5	0.152 ± 0.001	0.151 ± 0.001
	Meaze et al.	3/0	30.1993 ± 0.0306	40.3 ± 2.4	0.121 ± 0.060	0.120 ± 0.060
	Belanova et al.	—	30.08 ± 0.12	57.1 ± 16.6	0.15 ± 0.05	0.15 ± 0.05
	JENDL-4.0	3/0	30.02	55.0	0.140	0.139
	ENDF/B-VIII.0	4/0	30.0	55.0	0.110	0.110
8	Present work	4/0	34.196 ± 0.003	60.0 (fixed)	0.087 ± 0.001	0.087 ± 0.001
	Meaze et al.	4/0	34.4917 ± 0.0249	406.0 ± 3.3	0.791 ± 0.109	0.79 ± 0.11
	Belanova et al.	—	34.28 ± 0.15	60 ± 10	0.10 ± 0.02	0.10 ± 0.02
	JENDL-4.0	4/0	34.19	60.0	0.095	0.095
	ENDF/B-VIII.0	—	—	—	—	—
9	Present work	3/0	35.135 ± 0.002	53.4 ± 0.9	7.27 ± 0.06	5.55 ± 0.04
	Meaze et al.	3/0	35.2938 ± 0.0071	223.2 ± 3.3	3.415 ± 0.057	3.30 ± 0.05
	Belanova et al.	—	35.16 ± 0.20	70 ± 11	5.2 ± 0.6	4.4 ± 0.5
	Evans et al.	4/0	35.0	63 ± 6	6.92 ± 0.23	5.79 ± 0.18
	JENDL-4.0	3/0	35.14	69.0	8.00	6.32
	ENDF/B-VIII.0	3/0	35.2	65.0	5.30	4.47
10	Present work	4/0	35.905 ± 0.002	54.8 ± 1.0	8.89 ± 0.080	6.90 ± 0.06
	Meaze et al.	4/0	36.021 ± 0.022	251.7 ± 5.3	2.816 ± 0.077	2.76 ± 0.07
	Belanova et al.	—	35.95 ± 0.20	67 ± 8	6.63 ± 0.60	5.6 ± 0.4
	Evans et al.	4/0	35.8	71 ± 7	8.27 ± 0.28	6.85 ± 0.22
	Christensen	—	36.7 ± 0.3	-	36	—
	JENDL-4.0	4/0	35.9	65.0	8.00	6.56
	ENDF/B-VIII.0	4/0	35.9	65.0	8.44	6.86
11	Present work	4/0	39.117 ± 0.002	47.0 ± 0.5	27.3 ± 0.1	13.4 ± 0.1
	Meaze et al.	4/0	39.2182 ± 0.0080	561.2 ± 0.4	6.058 ± 0.515	5.94 ± 0.50
	Belanova et al.	—	39.2 ± 0.2	64 ± 10	23.0 ± 6.0	14.0 ± 2.4
	Evans et al.	4/0	39.0	64.3 ± 3.3	24.9 ± 0.5	14.7 ± 0.4
	Christensen	—	39.4 ± 0.5	—	27	—
	JENDL-4.0	4/0	39.1	60.0	24.9	14.3
	ENDF/B-VIII.0	3/0	39.13	60.0	22.4	12.1
12	Present work	3/0	49.113 ± 0.003	46.7 ± 4.2	0.531 ± 0.004	0.517 ± 0.038
	Meaze et al.	3/0	49.1832 ± 0.0001	49.357 ± 0.218	0.490 ± 0.001	0.479 ± 0.001
	Belanova et al.	—	49.23 ± 0.20	65.5 (fixed)	0.53 ± 0.07	0.52 ± 0.07
	JENDL-4.0	3/0	49.13	54	0.525	0.514
	ENDF/B-VIII.0	4/0	49.15	53	0.525	0.516
	Present work	4/0	57.53(fixed)	55(fixed)	0.140(fixed)	
	JENDL-4.0	4/0	57.53	55	0.140	
	ENDF/B-VIII.0	4/0	57.54	56	0.130	
	Present work	4/0	59.5 (fixed)	55(fixed)	0.065(fixed)	
	JENDL-4.0	4/0	59.05	55	0.065	
	ENDF/B-VIII.0	3/0	59.05	56	0.060	
13	Present work	4/0	63.094 ± 0.004	50.0 ± 2.3	2.90 ± 0.03	2.63 ± 0.03
	Meaze et al.	4/0	62.979 ± 0.0078	213.39 ± 18.74	1.918 ± 0.026	1.89 ± 0.03
	Belanova et al.	—	63.22 ± 0.30	65.5 (fixed)	2.30 ± 0.15	2.16 ± 0.13
	Evans et al.	4/0	62.9	62 ± 7	3.0 ± 0.2	2.8 ± 0.2
	JENDL-4.0	4/0	63.11	64	2.70	2.51
	ENDF/B-VIII.0	4/0	63.12	64	2.90	2.68

(Continued)

TABLE V (Continued)

Number	Reference	J/l	Resonance Energy (eV)	Γ_γ (meV)	$g\Gamma_n$ (meV)	Capture Kernel (meV)
14	Present work	4/0	76.834 ± 0.005	60.9 ± 2.6	6.28 ± 0.08	5.30 ± 0.07
	Meaze et al.	4/0	75.7992 ± 0.0027	36.216 ± 7.064	2.418 ± 0.034	2.16 ± 0.05
	Desjardins et al.	—	76.9 ± 0.2	69 ± 20	5.5 ± 0.9	4.8 ± 0.7
	JENDL-4.0	4/0	76.85	49.0	6.00	4.93
	ENDF/B-VIII.0	3/0	76.85	48.0	6.00	4.67
	Present work	4/0	77.61(fixed)	56 (fixed)	2.50(fixed)	
	JENDL-4.0	4/0	77.61	56.0	2.50	
	ENDF/B-VIII.0	4/0	77.64	54.0	2.80	
15	Present work	3/0	78.887 ± 0.007	55 (fixed)	0.693 ± 0.010	0.674 ± 0.009
	Meaze et al.	3/0	78.4992 ± 0.2838	30.456 ± 5.851	1.760 ± 0.001	1.55 ± 0.03
	Desjardins et al.	—	79.0 ± 0.2	—	1.1 ± 0.2	—
	JENDL-4.0	3/0	78.95	55.0	0.850	0.820
	ENDF/B-VIII.0	3/0	78.95	56.0	0.850	0.822
16	Present work	4/0	82.885 ± 0.005	48.6 ± 2.6	7.11 ± 0.12	5.64 ± 0.10
	Desjardins et al.	—	83.0 ± 0.2	58 ± 8	8 ± 1	6.4 ± 0.7
	Fluharty et al.	—	82.7 ± 1.4	—	5.5 ± 2.0	—
	JENDL-4.0	4/0	82.92	48	7.00	5.56
	ENDF/B-VIII.0	4/0	82.94	52	7.00	5.65
	Present work	3/0	85.1 (fixed)	58 (fixed)	2.15 (fixed)	
	JENDL-4.0	3/0	85.1	58 .0	2.15	
	ENDF/B-VIII.0	3/0	85.1	58.0	2.05	
	Present work	4/0	85.6 (fixed)	55 (fixed)	0.150 (fixed)	
	JENDL-4.0	4/0	85.6	55	0.150	
	ENDF/B-VIII.0	4/0	85.8	56	0.100	
17	Present work	3/0	89.574 ± 0.007	51 (fixed)	1.70 ± 0.02	1.58 ± 0.02
	Desjardins et al.	—	89.7 ± 0.2	55 ± 18	1.8 ± 0.2	1.7 ± 0.2
	Fluharty et al.	—	89.4 ± 1.9	—	2.2 ± 1.1	—
	JENDL-4.0	3/0	89.58	51	1.70	1.58
	ENDF/B-VIII.0	4/0	89.60	55	1.65	1.57
18	Present work	3/0	91.376 ± 0.008	55 (fixed)	1.16 ± 0.02	1.11 ± 0.01
	Desjardins et al.	—	91.5 ± 0.2	—	1.2 ± 0.1	—
	Fluharty et al.	—	91.4 ± 1.9	—	1.0 ± 0.5	—
	JENDL-4.0	3/0	91.4	55	1.15	1.10
	ENDF/B-VIII.0	4/0	91.44	56	1.15	1.11
19	Present work	4/0	96.942 ± 0.008	55 (fixed)	1.73 ± 0.02	1.64 ± 0.02
	Desjardins et al.	—	97.1 ± 0.2	—	2.0 ± 0.5	—
	JENDL-4.0	4/0	96.98	55.0	1.90	1.79
	ENDF/B-VIII.0	3/0	97.0	56.0	1.60	1.50
20	Present work	3/0	99.264 ± 0.006	50.4 ± 0.9	57.3 ± 0.2	15.9 ± 0.2
	Desjardins et al.	—	99.4 ± 0.2	50 ± 15	62.5 ± 12.5	16.2 ± 3.7
	Firk	—	98.8 ± 1.0	54 ± 32	58 ± 8	
	JENDL-4.0	3/0	99.2	50.0	61.0	16.1
	ENDF/B-VIII.0	4/0	99.32	50.0	57.5	18.9
	Present work	3/0	103.5 (fixed)	55 (fixed)	0.455 (fixed)	
	JENDL-4.0	3/0	103.5	55.0	0.455	
	ENDF/B-VIII.0	3/0	103.5	56.0	0.550	

(Continued)

TABLE V (Continued)

Number	Reference	J/l	Resonance Energy (eV)	Γ_γ (meV)	$g\Gamma_n$ (meV)	Capture Kernel (meV)
21	Present work	3/0	105.47 ± 0.01	39.8 ± 1.5	14.6 ± 0.2	7.94 ± 0.15
	Tsubone et al.	3/0	105.57	55 (fixed)	12.76 ± 0.07	9.04 ± 0.04
	Desjardins et al.	—	105.6 ± 0.2	46 ± 10	16 ± 2	8.9 ± 1.1
	JENDL-4.0	3/0	105.53	50.0	15.0	8.90
	ENDF/B-VIII.0	4/0	105.54	50.0	15.0	9.78
22	Present work	4/0	115.03 ± 0.01	44.9 ± 1.4	22.4 ± 0.3	11.9 ± 0.2
	Tsubone et al.	4/0	115.14	55 (fixed)	19.57 ± 0.10	11.99 ± 0.04
	Desjardins et al.	—	115.2 ± 0.2	39 ± 12	24 ± 3	11 ± 2
	JENDL-4.0	4/0	115.08	57.0	22.2	13.1
	ENDF/B-VIII.0	3/0	115.08	57.0	20.5	11.3
	Present work	3/0	118.3 (fixed)	55 (fixed)	1.20 (fixed)	
	JENDL-4.0	3/0	118.3	55.0	1.20	
	ENDF/B-VIII.0	4/0	118.3	56.0	1.20	
23	Present work	3/0	126.38 ± 0.01	46.6 ± 1.8	20.9 ± 0.3	10.3 ± 0.2
	Tsubone et al.	3/0	126.50	55 (fixed)	19.84 ± 0.10	10.87 ± 0.03
	Desjardins et al.	—	126.6 ± 0.2	53 ± 10	23 ± 2	12 ± 1
	JENDL-4.0	3/0	126.46	54.0	22.0	11.4
	ENDF/B-VIII.0	3/0	126.46	54.0	22.0	11.4
24	Present work	4/0	136.37 ± 0.01	40.6 ± 2.2	12.0 ± 0.3	7.89 ± 0.20
	Tsubone et al.	4/0	136.51	55 (fixed)	11.06 ± 0.07	8.15 ± 0.04
	Desjardins et al.	-	136.6 ± 0.3	53 ± 10	13 ± 3	9.1 ± 1.5
	JENDL-4.0	4/0	136.45	47.0	12.0	8.25
	ENDF/B-VIII.0	4/0	136.48	47.0	11.0	7.77
25	Present work	4/0	138.28 ± 0.01	78.9 ± 18.6	5.88 ± 0.4	5.19 ± 0.34
	Tsubone et al.	4/0	138.44	55 (fixed)	6.06 ± 0.05	5.06 ± 0.03
	Desjardins et al.	—	138.5 ± 0.3	66 ± 20	7 ± 1	5.9 ± 0.8
	JENDL-4.0	4/0	138.38	66.0	6.50	5.53
	ENDF/B-VIII.0	3/0	138.33	56.0	6.50	5.31
26	Present work	3/0	144.11 ± 0.03	55 (fixed)	0.770 ± 0.035	0.747 ± 0.033
	Tsubone et al.	3/0	144.3	55 (fixed)	8.00 ± 0.02	6.00 ± 0.01
	Desjardins et al.	—	144.3 ± 0.3	—	0.90 ± 0.15	—
	JENDL-4.0	3/0	144.24	55.0	9.00	6.55
	ENDF/B-VIII.0	4/0	144.2	56.0	0.900	0.875
27	Present work	4/0	148.24 ± 0.02	55 (fixed)	2.30 ± 0.07	2.14 ± 0.06
	Tsubone et al.	—	148.41	55 (fixed)	2.36 ± 0.03	2.19 ± 0.03
	Desjardins et al.	—	148.5 ± 0.3	—	2.4 ± 0.25	—
	JENDL-4.0	4/0	148.35	55.0	2.30	2.14
	ENDF/B-VIII.0	3/0	148.31	56.0	2.30	2.10
28	Present work	3/0	149.65 ± 0.02	55 (fixed)	3.03 ± 0.08	2.69 ± 0.06
	Tsubone et al.	—	149.88	55 (fixed)	2.85 ± 0.03	2.55 ± 0.02
	Desjardins et al.	—	149.5 ± 0.3	—	3.0 ± 0.3	—
	JENDL-4.0	3/0	149.8	55.0	2.90	2.59
	ENDF/B-VIII.0	4/0	149.7	56.0	2.75	2.53

*J and l are the spin and orbital angular momentum. The number in the first column corresponds to the resonance number in Fig. 13.

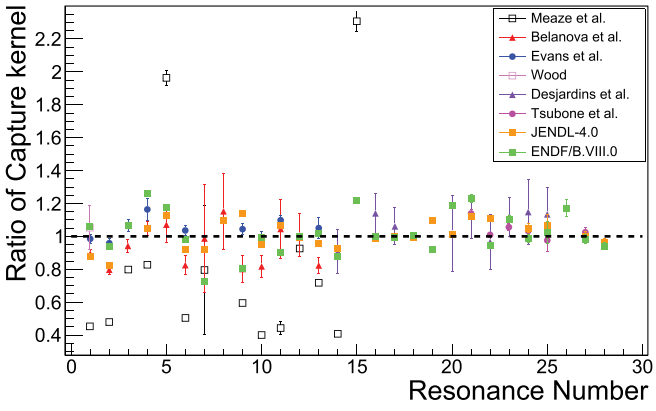

Fig. 13. Ratio of the capture kernel of the previous experiments and evaluated libraries to that of the present results. The resonance number is defined in Table V.

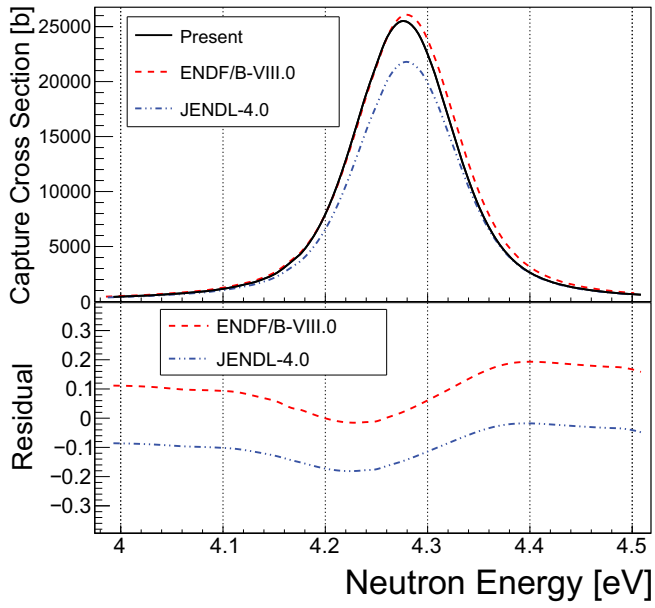

Fig. 14. Comparison of the capture cross section of the present results and evaluated libraries for the 4.3-eV resonance. The residual is defined as $(\sigma_{evaluation} - \sigma_{present})/\sigma_{present}$.

was roughly the same as that of ENDF/B-VIII.0, but the resonance energy was slightly different. In some resonances, the asymmetric shapes in the residual are found due to change of the resonance energy as seen at the 14-eV resonance.

VI. CONCLUSION

The neutron total and capture cross sections of natural Ta were measured at ANNRI of MLF in J-PARC to improve the accuracy of the resonance parameters of ^{181}Ta. Three natural Ta samples with thicknesses of 25 μm, 100 μm, and 2-mm were used in the transmission measurements, and a 6-μm-thick sample was used in the capture cross-section measurement. The PHWT was applied to derive the neutron capture cross section, and the thermal-neutron capture cross section was determined as $21.3 \pm 0.3\ (stat) \pm 0.6\ (sys)$ b. The resonance parameters of 28 resonances below 150 eV were evaluated from the simultaneous fit of the transmissions and the capture cross section using REFIT. This result will contribute to improve the reliability of the nuclear data library in the future.

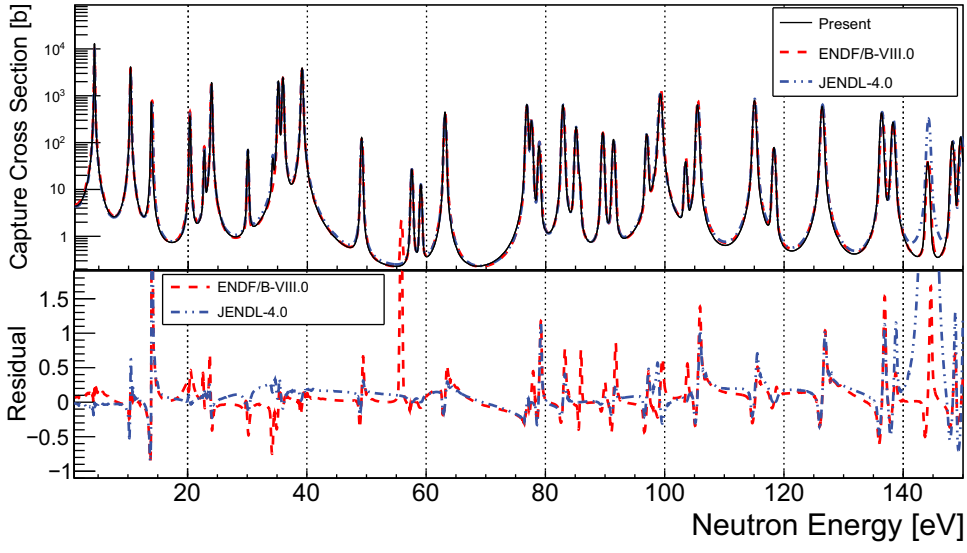

Fig. 15. Comparison of the capture cross section of the present results and evaluated libraries for the 4.3-eV resonance.

APPENDIX

ESTIMATION OF THE UNCERTAINTY ON THE BEAM INTENSITY FLUCTUATION CAUSED BY SCATTERING WITH THE AIR

Neutrons mainly react with the atoms of nitrogen (N), oxygen (O), and hydrogen (H) present in the air. The atomic density can be calculated from the atmospheric pressure P (Pa), the humidity R_H, and the temperature T (K). Assuming the ideal gas, the pressure was related to the molecular density n_m (mol/m^3) as

$$P = n_m RT \ , \tag{A.1}$$

where $R = 8.31$ (Pa · m^3/K · mol) is the gas constant. The saturated vapor pressure of water $e(T)$ (Pa) can be calculated approximately as[31]

$$e(T) = 610.78 \exp\left(\frac{17.27(T - 273.15)}{T - 35.85}\right) \ , \tag{A.2}$$

and the molecular density of water vapor in the air is calculated from Eq. (A.1) as

$$n_m^{H_2O} = R_H e(T)/RT \ . \tag{A.3}$$

where R_H is the humidity. Based on these formulas, the atomic densities n_N, n_O, and n_H (mol/m^3) were obtained as

$$n_N = 1.6P/RT \ , \tag{A.4}$$

$$n_O = 0.4P/RT + R_H e(T)/RT \ , \tag{A.5}$$

$$n_H = 2.0R_H e(T)/RT \ . \tag{A.6}$$

Here, the abundance ratio $O_2 : N_2 = 2 : 8$ was used. The transmission T_{air} passing the 7-m air region can be calculated from

$$T_{air} = \exp(-7(n_N\sigma_N + n_O\sigma_O + n_H\sigma_H)) \ , \tag{A.7}$$

where σ_N, σ_O, and σ_H are the total cross sections. In this estimation, the neutron energy dependence of the cross section was not considered, and the cross sections were used at thermal neutron energy. In these nuclei, the total cross section is almost flat from 0.1 to 150 eV because the potential scattering reaction is dominant and the resonances do not existed. Table A.I shows the transmission T_{air} in each atmospheric pressure and humidity at $T = 293.15$ K (20°C).

TABLE A.I

The Transmission of the Air Region T_{air}

		P(h·Pa)				
		980	990	1000	1010	1020
R_H (%)	20	0.702	0.700	0.697	0.695	0.692
	40	0.700	0.697	0.695	0.692	0.690
	60	0.697	0.695	0.692	0.690	0.687
	80	0.695	0.692	0.690	0.687	0.685
	100	0.692	0.689	0.687	0.685	0.682

If the humidity changes by 20% or the atmospheric pressure changes by 10 h·Pa, the transmission changes by about 0.3%. Based on observations at a weather station located near J-PARC, we determined that the humidity and the pressure may have varied about those during the experiment. It was therefore decided to add 0.3% as the beam intensity uncertainty.

Acknowledgments

The authors would like to thank the staff for their efforts in operating the accelerators and the neutron production target of MLF in J-PARC. The neutron experiments at ANNRI of MLF in J-PARC were performed under the user program (proposal numbers 2019P0100 and 2020P0100).

Disclosure Statement

No potential conflict of interest was reported by the author(s).

ORCID

Shunsuke Endo http://orcid.org/0000-0001-9100-6763
Atsushi Kimura http://orcid.org/0000-0002-1942-1724

References

1. "Application of the Concepts of Exclusion Exemption and Clearance," RS-G-1.7, IAEA Safety Standard Series, International Atomic Energy Agency (2004).
2. T. KAI et al., "Reliability Estimation of Neutron Resonance Thermometry Using Tantalum and Tungsten," *Physics Procedia*, **88**, 306 (2017); https://doi.org/10.1016/j.phpro.2017.06.042.

3. A. K. M. M. H. MEAZE, K. DEVAN, and M. U. KHANDAKER, "Measurements of the Neutron Total Cross-Sections of Tantalum by Using Pulsed Neutrons Based on an Electron Linac," *J. Korean Phys. Soc.*, **48**, 827 (2006).

4. N. M. LARSON, "Updated User's Guide for SAMMY: Multilevel R-Matrix Fits to Neutron Data Using Bayes' Equations," ORNL/TM–9179/R4, Oak Ridge National Laboratory (2008).

5. S. ENDO et al., "Measurements of Neutron Total and Capture Cross Sections of Niobium-93 Below 400 eV," *J. Nucl. Sci. Technol.*, **59**, *3*, 318 (2021); https://doi.org/10.1080/00223131.2021.1970040.

6. T. S. BELANOVA, A. G. KOLESOV, and V. A. PORUCHIKOV, "Study on Neutron Resonances of ^{181}Ta in the Neutron Energy Range from 2 to 70 eV," *At. Ehnergiya*, **38**, 430 (1975).

7. J. E. EVANS et al., "Radiation Widths of Neutron Resonances in Ta," *Nucl. Phys.*, **9**, *2*, 205 (1958); https://doi.org/10.1016/0029-5582(58)90392-4.

8. J. E. LYNN and E. R. RAE, "The Analysis of Neutron Spectrometer Resonance Data," *J. Nucl. Energy*, **4**, 418 (1957).

9. R. L. CHRISTENSEN, "Slow Neutron Resonance in Tantalum," *Phys. Rev.*, **92**, *6*, 1509 (1953); https://doi.org/10.1103/PhysRev.92.1509.

10. R. E. WOOD, "Slow-Neutron Resonance Scattering in Ag, Au, and Ta," *Phys. Rev.*, **104**, *5*, 1425 (1956); https://doi.org/10.1103/PhysRev.104.1425.

11. S. F. MUGHABGHAB and D. J. GARBER, *Neutro Cross Sections. Volume 1. Resonance Parameters*, Brookhaven National Laboratory (1973).

12. K. H. HARA et al., "Neutron Transmission Measurement and Simulation of Ta-181 for Neutron Resonance Thermometry," *Proc. 2019 IEEE Nuclear Science Symp. and Medical Imaging Conf. (NSS/MIC)*, Manchester, United Kingdom, October 26–November 2, 2019, Institute of Electrical and Electronics Engineers (2019).

13. K. SHIBATA et al., "JENDL-4.0: A New Library for Nuclear Science and Technology," *J. Nucl. Sci. Technol.*, **48**, *1*, 1 (2011); https://doi.org/10.1080/18811248.2011.9711675.

14. D. BROWN et al., "ENDF/B-VIII.0: The 8th Major Release of the Nuclear Reaction Data Library with CIELO-Project Cross Sections, New Standards and Thermal Scattering Data," *Nucl. Data Sheets*, **148**, *1*, 2018.

15. F. CORTE and A. SIMONITS, "Compilation of Accurately Measured 2200 m/s Cross-Sections for ^{181}Ta(n,γ) Reactions of Interest in Activation Analysis; A Critical Comparison with Literature," *Proc. Int. Conf. Nuclear Data for Science and Technology*, Mito, Japan, May 30–June 3, 1988, Japan Atomic Energy Research Institute (1988).

16. F. F. ARBOCCO et al., "Experimental Determination of K_0, Q_0 Factors, Effective Resonance Energies and Neutron Cross-Sections for 37 Isotopes of Interest in NAA," *J. Radional. Nucl. Chem.*, **302**, *1*, 655 (2014); https://doi.org/10.1007/s10967-014-3281-0.

17. S. NAKAMURA et al., "Thermal-Neutron Capture Cross-Section Measurement of Tantalum-181 Using Graphite Thermal Column at KUR," *J. Nucl. Sci. Technol.*, **58**, *10*, 1061 (2021); https://doi.org/10.1080/00223131.2021.1908187.

18. R. E. SCHMUNK, P. D. RANDOLPH, and R. M. BRUGGER, "Total Cross Sections of Ti, V, Y, Ta, and W," *Nucl. Sci. Eng.*, **7**, *2*, 193 (1960); https://doi.org/10.13182/NSE60-A29090.

19. M. C. MOXON, T. C. WARE, and C. J. DEAN, "REFIT-2009, Multilevel Resonance Parameter Least Square Fit of N Transmission, Capture, Fission & Self Indication Data," NEA-0914/08, Organisation for Economic Co-operation and Development, Nuclear Energy Agency (2011).

20. A. KIMURA et al., "Measurements of the ^{243}Am Neutron Capture and Total Cross Sections with ANNRI at J-PARC," *J. Nucl. Sci. Technol.*, **56**, *6*, 479 (2019); https://doi.org/10.1080/00223131.2019.1598508.

21. K. TERADA et al., "Measurements of Neutron Total and Capture Cross Sections of ^{241}Am with ANNRI at J-PARC," *J. Nucl. Sci. Technol.*, **55**, *10*, 1198 (2018); https://doi.org/10.1080/00223131.2018.1485519.

22. R. L. MACKLIN and J. H. GIBBONS, "Capture-Cross-Section Studies for 30-220 keV Neutrons Using a New Technique," *Phys. Rev.*, **159**, *4*, 1007 (1967); https://doi.org/10.1103/PhysRev.159.1007.

23. K. KINO et al., "Energy Resolution of Pulsed Neutron Beam Provided by the ANNRI Beamline at the J-PARC/MLF," *Nucl. Instrum. Methods Phys. Res. Sect. A*, **736**, 66 (2014); https://doi.org/10.1016/j.nima.2013.09.060.

24. T. SATO et al., "Features of Particle and Heavy Ion Transport Code System (PHITS) Version 3.02," *J. Nucl. Sci. Technol.*, **55**, *6*, 684 (2018); https://doi.org/10.1080/00223131.2017.1419890.

25. J. S. DESJARDINS et al., "Slow Neutron Resonance Spectroscopy. II. Ag, Au, Ta," *Phys. Rev.*, **120**, *6*, 2214 (1960); https://doi.org/10.1103/PhysRev.120.2214.

26. R. G. FLUHARTY, F. B. SIMPSON, and O. D. SIMPSON, "Neutron Resonance Measurements of Ag, Ta, and U^{238}," *Phys. Rev.*, **103**, *6*, 1778 (1956); https://doi.org/10.1103/PhysRev.103.1778.

27. F. W. K. FIRK, "Neutron Resonances Parameters of Tantalum from 20 to 100 eV," *Nucl. Phys.*, **9**, *2*, 198 (1958); https://doi.org/10.1016/0029-5582(58)90391-2.

28. I. TSUBONE, Y. NAKAJIMA, and Y. KANDA, "Resonance Parameters of Tantalum-181 in Neutron Energy Range from 100 to 4,300 eV," *J. Nucl. Sci.*

Technol., **24**, *12*, 975 (1987); https://doi.org/10.1080/18811248.1987.9733533.

29. G. N. KIM et al., "Measurement of Photoneutron Spectrum at Pohang Neutron Facility," *Nucl. Instrum. Methods Phys. Res. Sect. A*, **485**, *3*, 458 (2002); https://doi.org/10.1016/S0168-9002(01)02115-5.
30. L. B. BORST and V. L. SAILOR, "Neutron Measurements with the Brookhaven Crystal Spectrometer," *Rev. Sci. Instrum.*, **24**, *2*, 141 (1953); https://doi.org/10.1063/1.1770642.
31. O. TETENS, "Über Einige Meteorologische Begriffe," *Z. Geophys.*, **6**, 207 (1930).